

# Modeling the elastic properties and damage evolution in Ti–Al<sub>3</sub>Ti metal–intermetallic laminate (MIL) composites

Tiezheng Li<sup>a,b</sup>, F. Grignon<sup>a</sup>, D.J. Benson<sup>a</sup>, K.S. Vecchio<sup>a</sup>, E.A. Olevsky<sup>b</sup>,  
Fengchun Jiang<sup>a</sup>, A. Rohatgi<sup>a</sup>, R.B. Schwarz<sup>c</sup>, M.A. Meyers<sup>a,\*</sup>

<sup>a</sup> Department of Mechanical and Aerospace Engineering, University of California, San Diego, La Jolla, CA 92093-0411, USA

<sup>b</sup> Mechanical Engineering Department, San Diego State University, San Diego, CA 92182-1323, USA

<sup>c</sup> Los Alamos National Laboratory, Los Alamos, NM 87545, USA

Received 6 June 2003; received in revised form 5 September 2003

## Abstract

The mechanical performance of Ti–Al<sub>3</sub>Ti metal–intermetallic laminate (MIL) composites synthesized by a reactive foil sintering technique was evaluated. The elastic properties and anisotropy of the laminates were calculated and successfully compared with resonant ultrasonic spectroscopy (RUS) measurements. The effect of internal stresses due to differences in the thermal expansion coefficient on fracture toughness was analyzed. The principal mechanisms of damage initiation and accumulation were identified experimentally. The compressive strength was modeled by FEM using the Johnson–Holmquist constitutive equation. The computed results were successfully compared with experiments. © 2003 Elsevier B.V. All rights reserved.

**Keywords:** Laminate composites; Mechanical performance; Damage evolution; FEM modeling

## 1. Introduction

Laminate composites are being intensively studied for a number of potential applications: electronic devices, structural components, armor, etc. Ceramic–ceramic [1], metal–ceramic [2], metal–metal [3], metal–ceramic–intermetallic [4] and metal–intermetallic [5] systems have shown desirable properties. In particular, the Ti–Al<sub>3</sub>Ti system has a great potential for structural applications because of its low density and excellent specific mechanical properties [6]. Rawers and co-workers [7–12] demonstrated that these intermetallics could be synthesized by high temperature synthesis reaction. This system has been extensively investigated by Harach and Vecchio [13], who introduced a number of significant advances. Whereas Rawers and co-workers [7–12] used a vacuum or argon protective atmosphere, Harach and Vecchio [13] were able to synthesize the laminates in open air. This represents a great technological advantage, since it enables industrial production at significant cost reduction.

The MIL process [6] consists of stacking aluminum and titanium foils in alternating layers, and placing them in the composite synthesis apparatus. The foil stack is then placed between two cartridge-heated nickel alloy platens and attached to the crosshead of a screw-driven load frame. Pressure and heating are applied in open air. The initial pressure is 3.8 MPa. The temperature is increased from 298 to 898 K, where it is kept for 2–3 h. This enables diffusion bonding of the layers. The temperature is then raised to 928 K. The initiation of reaction leads to a decrease in pressure. It drops to 1.5 MPa as a result of the formation of a liquid phase. At the completion of reaction, the pressure is again increased to 3.5 MPa. The pressure/temperature excursion in this MIL process is selected such that the aluminum reacts completely and no gaps are left in the final product. The thickness of the initial Al and Ti alloy sheets is selected in such a manner as to produce the desired thickness and ratios between the final phases. The foil dimensions are selected to completely consume the aluminum in forming the intermetallic compound Al<sub>3</sub>Ti with alternating layers of partially unreacted Ti metal.

The goal of the work whose results are presented herein is to provide a broad understanding of the mechanical response (elastic, plastic, and damage evolution) of this metal–intermetallic system. This knowledge is important in

\* Corresponding author. Tel.: +1-619-534-4719;  
fax: +1-619-534-5698.

E-mail address: mameyers@mae.ucsd.edu (M.A. Meyers).

**Nomenclature**

$a_{ij}$	the cosines of the orientation angle $\beta$
$c(h_m/H)$	the concentrations of Ti
$D$	damage variable ranging from 0.0 to 1.0
$E_I$	the Young's modulus of intermetallic $Al_3Ti$
$E_{jj}$	the Young's modulus in direction $j$ for the composite
$E_m$	the Young's modulus of Ti
$G_{ij}$	the shear modulus in the $ij$ plane for the composite
$G_I$	the shear modulus of $Al_3Ti$
$G_m$	the shear modulus of Ti
$h(x/a, \alpha)$	the weight function
$K_0$	the crack-initiation toughness of the laminate composites
$K_{c,app}$	the measured toughness in the computation
$K_I$	the bulk modulus of $Al_3Ti$
$K_m$	the bulk modulus of Ti
$K_T$	the stress intensity due to the designed residual stresses of the laminate composites
$P_{HEL}$	the Hugoniot elastic limit (HEL) pressure
$P^*$	the normalized pressure
$S_{ij}$	the elastic compliance in the second-order tensor notation in the original coordinate system
$S_{mnop}$	the elastic compliance in the fourth-order tensor notation in the original coordinate system
$S'_{ij}$	the elastic compliance in the second-order tensor notation in the rotated coordinate system
$S'_{ijkl}$	the elastic compliance in the fourth-order tensor notation in the rotated coordinate system
$T$	the maximum tensile hydrostatic pressure
<i>Greek letters</i>	
$\alpha_{Al_3Ti}$	the thermal expansion coefficient of $Al_3Ti$
$\alpha_{Ti}$	the thermal expansion coefficient of Ti
$\beta$	the angle with respect to the three-axis of the coordinate system
$\dot{\varepsilon}^*$	the normalized strain rate
$\Delta\varepsilon_0$	the strain mismatch of the laminate composites
$\sigma_{HEL}$	the Hugoniot elastic limit stress
$\sigma_r(x)$	the residual stresses of the laminate composites
$\sigma^*$	the normalized equivalent stress
$\sigma_f^*$	normalized fractured strength
$\sigma_{in}^*$	normalized intact strength
$\nu_{ij}$	the Poisson's ratio in the $ij$ plane for the composite
$\nu_I$	the Poisson's ratio of intermetallic $Al_3Ti$
$\nu_m$	the Poisson's ratio of Ti

the computational modeling of the response of the composite to external loading, especially in the case of ballistic impact. Thus, the work presented herein has the following experimental components.

- Determination of elastic anisotropy of Ti– $Al_3Ti$  MIL composites.
- Determination of stress intensity of the laminate.
- Damage observation in specimens.

This experimental work was used in the development of a computational framework. The following aspects are addressed.

- The physical modeling of damage evolution.
- The finite element computational modeling.

This quantitative framework of the mechanical behavior is essential for the development and implementation of computational methods that enable optimization of laminate parameters for specific structural applications.

## 2. Elastic properties of Ti– $Al_3Ti$ metal–intermetallic laminate (MIL) composites

### 2.1. Elastic properties of Ti– $Al_3Ti$ metal–intermetallic laminate composite as a function of volume fraction of Ti

Relationships from Christensen [14] and Calcote [15] were used to calculate the elastic properties of laminates. Fig. 1 shows the coordinate system for the Ti– $Al_3Ti$  metal–intermetallic laminate composites. The [100] direction is perpendicular to the laminate plane ( $OX_1$ ). The material is isotropic in the  $OX_2X_3$  plane. The equations that express the change in elastic properties as a function of volume fraction of Ti are

$$E_{11} = 2(1 - \nu_m + (\nu_m - \nu_I)(1 - c)) \times \left[ (1 - c) \frac{K_m(2K_I + G_I) - G_I(K_m - K_I)(1 - c)}{2K_I + G_I + 2(K_m - K_I)(1 - c)} + c \frac{K_m(2K_I + G_m) + G_m(K_I - K_m)(1 - c)}{2K_I + G_m - 2(K_I - K_m)(1 - c)} \right] \quad (1)$$

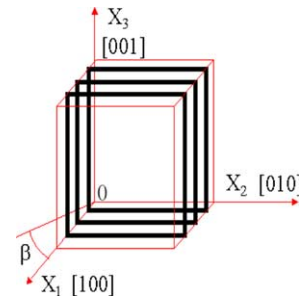


Fig. 1. Ti– $Al_3Ti$  metal–intermetallic laminate composites coordinate system with angle  $\beta$  about the three-axis.

$$E_{22} = cE_m + (1 - c)E_1 + \frac{c(1 - c)E_1E_m(\nu_m - \nu_1)^2}{cE_m(1 - \nu_1^2) + (1 - c)E_1(1 - \nu_m^2)} \quad (2)$$

$$G_{12} = (1 - c)G_1 \frac{2G_m - (G_m - G_1)(1 - c)}{2G_1 + (G_m - G_1)(1 - c)} + cG_m \frac{(G_m + G_1) - (G_m - G_1)(1 - c)}{(G_m + G_1) + (G_m - G_1)(1 - c)} \quad (3)$$

$$\nu_{23} = \frac{c\nu_m E_m(1 - \nu_1^2) + (1 - c)\nu_1 E_1(1 - \nu_m^2)}{cE_m(1 - \nu_1^2) + (1 - c)E_1(1 - \nu_m^2)} \quad (4)$$

$$\nu_{12} = \frac{(1 - c)K_m \nu_m (2K_1 + G_1)c + K_1 \nu_1 (2K_m + G_1)(1 - c)}{K_m(2K_1 + G_1) - G_1(K_m - G_1)(1 - c)} + c \frac{K_1 \nu_1 (2K_m + G_m)(1 - c) + K_m \nu_m (2K_1 + G_m)c}{K_m(2K_1 + G_m) + G_m(K_1 - K_m)(1 - c)} \quad (5)$$

Table 1  
Young's modulus, shear modulus and Poisson's ratio of Al<sub>3</sub>Ti and Ti

	Ti	Al <sub>3</sub> Ti
<i>E</i> (GPa)	115.7	216
<i>G</i> (GPa)	43.8	92.3
<i>ν</i>	0.321	0.17

$$G_{23} = \frac{E_{22}}{2(1 + \nu_{23})} \quad (6)$$

where  $E_{jj}$  is the Young's modulus in direction  $j$  for the composite;  $G_{ij}$  the shear modulus in the  $ij$  plane for the composite;  $\nu_{ij}$  the Poisson's ratio in the  $ij$  plane for the composite;  $\nu_m$  the Poisson's ratio of Ti;  $\nu_1$  the Poisson's ratio of intermetallic Al<sub>3</sub>Ti;  $c(h_m/H)$  the concentrations of Ti;  $E_m$  the Young's Modulus of Ti;  $E_1$  the Young's Modulus of intermetallic Al<sub>3</sub>Ti;  $K_m$  and  $K_1$  the bulk moduli of Ti and intermetallic Al<sub>3</sub>Ti, respectively;  $G_m$  and  $G_1$  are the shear moduli.

The corresponding strain-stress relation is

$$\begin{Bmatrix} \varepsilon_{11} \\ \varepsilon_{22} \\ \varepsilon_{33} \\ 2\varepsilon_{23} \\ 2\varepsilon_{31} \\ 2\varepsilon_{12} \end{Bmatrix} = \begin{bmatrix} \frac{1}{E_{11}} & -\frac{\nu_{12}}{E_{11}} & -\frac{\nu_{12}}{E_{11}} & 0 & 0 & 0 \\ -\frac{\nu_{12}}{E_{11}} & \frac{1}{E_{22}} & -\frac{\nu_{23}}{E_{22}} & 0 & 0 & 0 \\ -\frac{\nu_{12}}{E_{11}} & -\frac{\nu_{23}}{E_{22}} & \frac{1}{E_{22}} & 0 & 0 & 0 \\ 0 & 0 & 0 & \frac{2(1 + \nu_{23})}{E_{22}} & 0 & 0 \\ 0 & 0 & 0 & 0 & \frac{1}{G_{12}} & 0 \\ 0 & 0 & 0 & 0 & 0 & \frac{1}{G_{12}} \end{bmatrix} \begin{Bmatrix} \sigma_{11} \\ \sigma_{22} \\ \sigma_{33} \\ \sigma_{23} \\ \sigma_{31} \\ \sigma_{12} \end{Bmatrix} \quad (7)$$

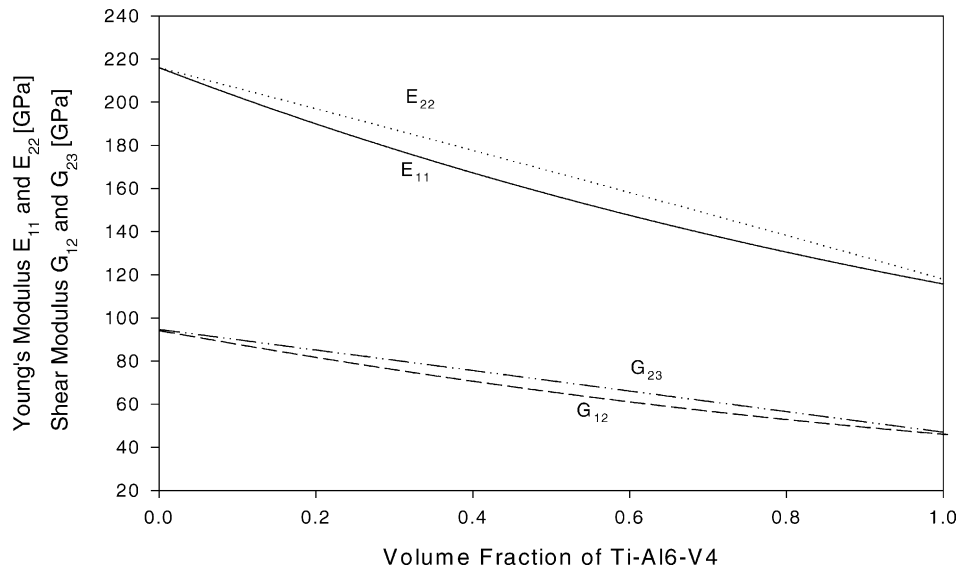


Fig. 2. Elastic properties, Young's and shear moduli of the laminate composites as a function of volume fraction of Ti.

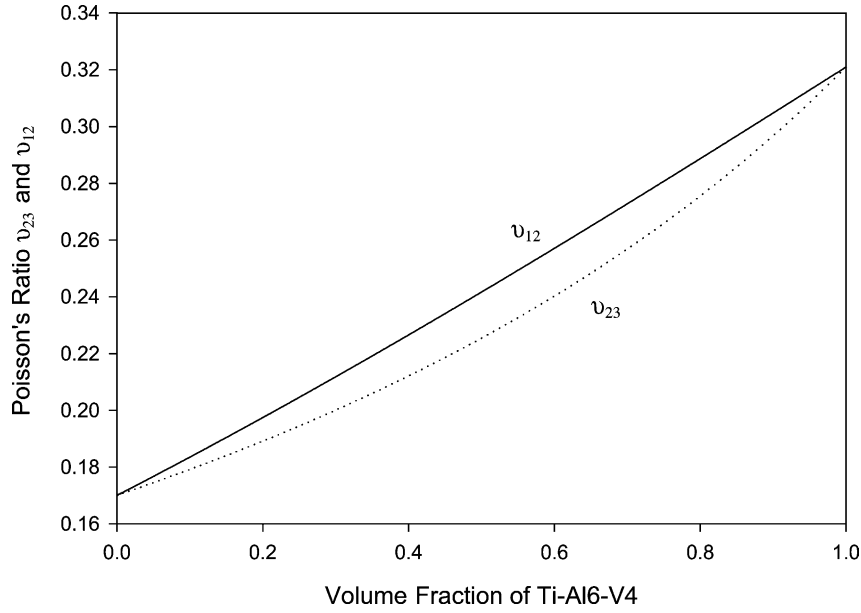


Fig. 3. Poisson's ratios  $\nu_{12}$  and  $\nu_{23}$  of the laminate composites as a function of volume fraction of Ti.

The Young's modulus, shear modulus and Poisson's ratio of  $\text{Al}_3\text{Ti}$  and Ti are given in Table 1; these values were obtained from the literature [16].

Figs. 2 and 3 represent the calculated Young's moduli ( $E_{11}$  and  $E_{22}$ ), shear moduli ( $G_{12}$  and  $G_{23}$ ) and Poisson's ratios ( $\nu_{12}$  and  $\nu_{23}$ ) of the laminate composites as a function of volume fraction of Ti.

The calculated values agree very well with the experimental results shown in Table 2, obtained for 80%  $\text{Al}_3\text{Ti}$  and 20% Ti by resonant ultrasonic spectroscopy (RUS) at Los Alamos National Laboratory.

## 2.2. Elastic properties of Ti– $\text{Al}_3\text{Ti}$ metal–intermetallic laminate composites as a function of orientation

The same coordinate system was used;  $X_1[100]$  is the transverse direction and  $\beta$  is the angle with respect to the three-axis (transformed  $[100]$  axis creates an angle  $\beta$  with the original  $[100]$  axis). The elastic moduli in different orientations can be calculated by expressing the

elastic compliances in the fourth-order tensor notation, and transforming this tensor [17] according to

$$S'_{ijkl} = a_{im}a_{jn}a_{ko}a_{lp}S_{mnop} \quad (8)$$

where  $a_{ij}$  are the cosines of the orientation angles:  $a_{11} = \cos \beta$ ,  $a_{12} = 0$ ,  $a_{13} = \sin \beta$ ,  $a_{21} = -\sin \beta$ ,  $a_{22} = 0$ ,  $a_{23} = \cos \beta$ ,  $a_{31} = 0$ ,  $a_{32} = 1$ , and  $a_{33} = 0$ . The composition 80%  $\text{Al}_3\text{Ti}$  and 20% Ti is used in this calculation. In converting the elastic compliances from two-index notation to the tensorial four-index notation, one has to carefully consider factors of 2 and 4 arising from the definition of strain. Knowing the elastic compliance tensor in the rotated coordinate system, the elastic moduli can be obtained from

$$E_{11}(\beta) = \frac{1}{S'_{11}(\beta)} \quad (9)$$

$$E_{22}(\beta) = \frac{1}{S'_{22}(\beta)} \quad (10)$$

$$G_{12}(\beta) = \frac{1}{S'_{66}(\beta)} \quad (11)$$

$$G_{23}(\beta) = \frac{1}{S'_{44}(\beta)} \quad (12)$$

$$\nu_{12}(\beta) = \frac{-S'_{12}(\beta)}{S'_{11}(\beta)} \quad (13)$$

$$\nu_{23}(\beta) = \frac{-S'_{23}(\beta)}{S'_{22}(\beta)} \quad (14)$$

Table 2

Comparison of calculated and experimental elastic constants for Ti– $\text{Al}_3\text{Ti}$  metal–intermetallic laminate composites with 20% Ti

	Experimental data	Calculated data
$E_{11}$ (GPa)	186.98	189.96
$E_{22}$ (GPa)	180.92	196.45
$G_{12}$ (GPa)	73.94	79.76
$G_{23}$ (GPa)	74.50	82.60
$\nu_{12}$	0.1952	0.1974
$\nu_{23}$	0.2145	0.1895

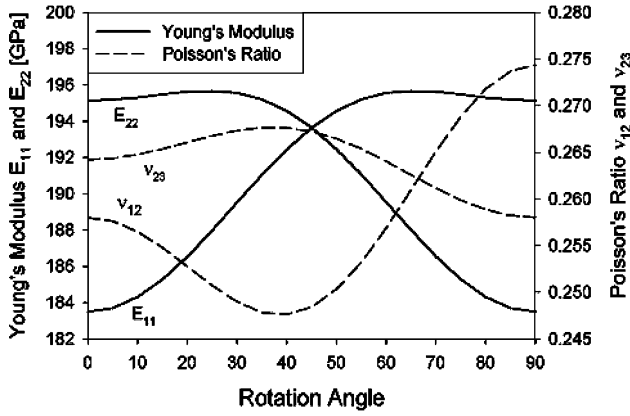


Fig. 4. Elastic properties of Ti–Al<sub>3</sub>Ti metal–intermetallic laminate composites as a function of orientation.

where

$$S'_{11}(\beta) = S_{11} \cos^4 \beta + S_{33} \sin^4 \beta + S_{55} \cos^2 \beta \sin^2 \beta + 2S_{31} \cos^2 \beta \sin^2 \beta$$

$$S'_{22}(\beta) = S_{33} \cos^4 \beta + S_{11} \sin^4 \beta + S_{55} \cos^2 \beta \sin^2 \beta + 2S_{31} \cos^2 \beta \sin^2 \beta$$

$$S'_{12}(\beta) = S_{13} \cos^4 \beta + S_{13} \sin^4 \beta + S_{11} \cos^2 \beta \sin^2 \beta + S_{33} \cos^2 \beta \sin^2 \beta - S_{55} \cos^2 \beta \sin^2 \beta$$

$$S'_{23}(\beta) = S_{32} \cos^2 \beta + S_{12} \sin^2 \beta$$

$$S'_{44}(\beta) = S_{44} \cos^2 \beta + S_{66} \sin^2 \beta$$

$$S'_{66}(\beta) = S_{55} \cos^4 \beta + S_{55} \sin^4 \beta + 4S_{33} \cos^2 \beta \sin^2 \beta - 4S_{31} \cos^2 \beta \sin^2 \beta - 2S_{55} \cos^2 \beta \sin^2 \beta$$

The compliance matrix can be calculated from its relationship with the stiffness matrix ( $C \cdot S = 1$ ), as obtained from the resonant ultrasonic spectroscopy [17] result.

As shown in Fig. 4, the Young's modulus  $E_{11}$  is a mirror of  $E_{22}$ ; they are equal to each other at  $\beta = 45^\circ$ . For an increasing  $\beta$ ,  $E_{22}$  first increases and then rapidly decreases. The results in Fig. 4 show the anisotropy in the elastic properties of this laminate system, which in turn affect its mechanical properties in a significant manner.

### 3. Toughness of Ti–Al<sub>3</sub>Ti metal–intermetallic laminate composites

Mechanical properties can be improved by an imposed distribution of internal stresses. This can be considered as a global materials design principle. This methodology has been implicitly applied in a number of previous studies [18–20]. From the modeling viewpoint, the effect of the internal stresses can be interpreted in one of two ways. In one

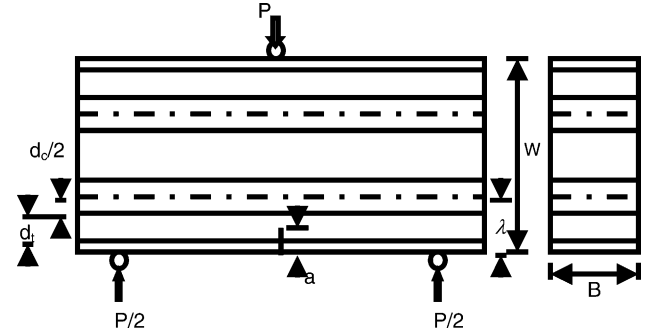


Fig. 5. Schematic of a multilayer single-edge-notch-bend specimen, adapted from [23].

interpretation, the effect of the macroscopic residual stress can be treated entirely as a correction to the crack-driving force, and the intrinsic fracture toughness of the material is considered unchanged from that of a monolithic material. This approach was used by Sherman and Gong [20] and Green [21] to treat the fracture of compression-strengthened glass and three-layer alumina–zirconia composites, respectively. Alternatively, a surface-compression-strengthened ceramic can be considered to be a toughened ceramic since the resistance to fracture from a surface crack is enhanced by the presence of the surface compression [22]. In this case, the enhanced fracture toughness must be viewed as apparent fracture toughness since the higher resistance to fracture is derived from a reduction of the crack-driving force rather than an increase in the intrinsic resistance to crack extension.

Fig. 5 shows a schematic of a multilayer single-edge-notch-bend specimen. The beam width is denoted as  $W$ , the span is  $S$ , the width is  $B$  and the normal force is  $P$ . Since the components of the composites have different thermal expansion coefficients, one of the components is under compression and the other is under tension and the thickness of the compression layer is  $d_c$ , while the thickness of the tension layer is  $d_t$ . The measured toughness  $K_{c,app}$ , for a given loading condition can be predicted by

$$K_{c,app} = K_0 + K_T \quad (15)$$

where  $K_0$  is taken to be the crack-initiation toughness of the composite and  $K_T$  is the stress intensity due to the designed residual stresses, obtained by integrating the product of the stress distribution and a weight function over the crack length [24,25]. A weight function method is used to calculate  $K_T$ , and then the apparent fracture toughness was obtained from the crack-initiation toughness as follows:

$$K_T = \int_0^a h \left( \frac{x}{a, \alpha} \sigma_r(x) dx \right) \quad (16)$$

where  $a$  is the crack length,  $\alpha$  the crack length normalized by specimen's width  $W$ ,  $h(x/a, \alpha)$  is the weight function and can be calculated for a known crack and laminate geometry

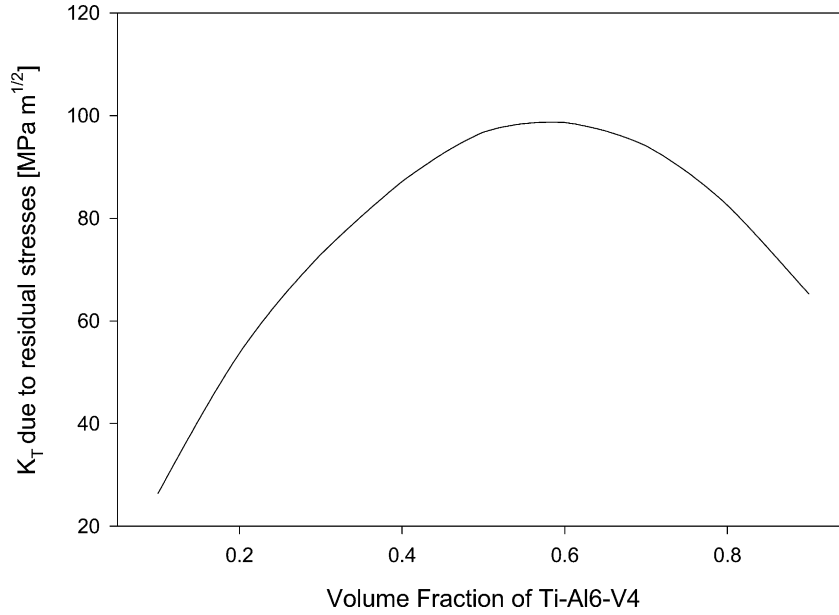


Fig. 6. Stress intensity of three-layer laminate due to the residual stresses as a function of fraction of Ti.

[26].  $h(x/a, \alpha)$  is given as

$$h\left(\frac{x}{a}, \alpha\right) = \sqrt{\frac{2}{\pi a}} \frac{1}{(1-x/a)^{1/2}(1-\alpha)^{3/2}} \times \left\{ (1-\alpha)^{3/2} + \sum A_{\nu\mu} \left(1 - \frac{x}{a}\right)^{\nu+1} \alpha^\mu \right\} \quad (17)$$

$A_{\nu\mu}$  is given in Table 3. The following values are used in the calculation:  $a = 11.9$  mm,  $W = 20.68$  mm, and  $\alpha = 0.575$ .

The simplest structure, a symmetric three-layer laminate is analyzed. The residual stresses,  $\sigma_r(x)$  [22], due to a strain mismatch are given by

$$\sigma_r(x) = \begin{cases} \sigma_1 = -\frac{\Delta\varepsilon_0 d_2 E_1}{W^*(1-\gamma_1)} & 0 \leq x \leq d_1 \\ \sigma_2 = \frac{2\Delta\varepsilon_0 d_1 E_1}{W^*(1-\gamma_1)} & d_1 \leq x \leq d_1 + d_2 \\ \sigma_1 = -\frac{\Delta\varepsilon_0 d_2 E_1}{W^*(1-\gamma_1)_2} & d_1 + d_2 \leq x \leq 2d_1 + d \end{cases} \quad (18)$$

where the subscripts 1 and 2 represent Ti and  $\text{Al}_3\text{Ti}$ , respectively, and

$$W^* = 2\xi d_1 + d_2$$

Table 3  
The value of  $A_{\nu\mu}$  in the weight function

	$\mu = 0$	$\mu = 1$	$\mu = 2$	$\mu = 3$	$\mu = 4$
$\nu = 0$	0.498	2.4463	0.07	1.3187	-3.067
$\nu = 1$	0.5416	-5.0806	24.3447	-32.7208	18.1214
$\nu = 2$	-0.19277	2.55863	-12.6415	19.763	-10.986

$$\xi = \frac{1 - \gamma_2 \frac{E_1}{E_2}}{1 - \gamma_1}$$

$\Delta\varepsilon_0$  is the strain mismatch. The Ti layers are under compression due to the high thermal expansion coefficient of  $\text{Al}_3\text{Ti}$  ( $\alpha_{\text{Ti}} = 9.5 \times 10^{-6} \text{ K}^{-1}$  and  $\alpha_{\text{Al}_3\text{Ti}} = 13 \times 10^{-6} \text{ K}^{-1}$ )

$$\Delta\varepsilon_0 = |(\alpha_{\text{Ti}} - \alpha_{\text{Al}_3\text{Ti}}) \Delta T| \quad (19)$$

where  $\Delta T$  is taken as 700 K [13]. Based on this data,  $\Delta\varepsilon_0 = 0.00245$ . Using Eqs. (16)–(19), the dependence of stress intensity of a three-layer laminate due to the residual stress is obtained as a function of volume fraction of Ti (from 0.1 to 0.9). The result, given in Fig. 6, shows that the stress intensity in a three-layer laminate caused by residual stress first increases and then decreases. The maximum value occurs when the fraction of Ti is about 57%. Previous experiments [6] showed that the initial toughness varied from 42 to 62  $\text{MPa}\sqrt{m}$  for 20% Ti and 35% Ti, thus according to Eq. (15),  $K_{c,\text{app}}$  for 20% Ti and 35% Ti can be obtained as  $92\text{MPa}\sqrt{m}$  and  $137\text{MPa}\sqrt{m}$ , respectively, which compared well with the steady-state toughness values (experimental data) of 80 and  $115\text{MPa}\sqrt{m}$ .

#### 4. Damage evolution in Ti– $\text{Al}_3\text{Ti}$ metal–intermetallic laminate composites: optical and SEM observations

A large number of compression tests were performed on the Ti–6Al–4V– $\text{Al}_3\text{Ti}$  metal–intermetallic laminate composites and some of the mechanisms have been discussed in the paper by Rohatgi et al. [6]. The tested samples were characterized in order to understand damage evolution as a function of volume fraction of titanium (from 0.14 to 0.50), of strain rate (from 0.0001 to 2800/s), and of the loading

Table 4  
Compression tested samples

Volume fraction of Ti-6-4 (%)	Loading direction to the laminate plane	Strain rate ( $s^{-1}$ )
14	Perpendicular	0.0001
14	Perpendicular	2800
14	Parallel	0.0001
14	Parallel	0.01
14	Parallel	2100
50	Perpendicular	0.0001
50	Perpendicular	1300
50	Perpendicular	2500
50	Parallel	0.0001

direction (compressive loading, parallel and perpendicular to the laminate planes). Optical and SEM observations have been performed on the tested samples shown in Table 4.

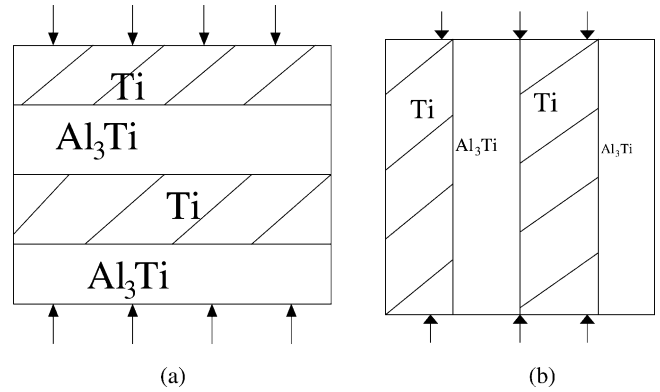


Fig. 7. Loading configuration: (a) compression loading perpendicular to the laminate plane; (b) compression loading parallel to the laminate plane.

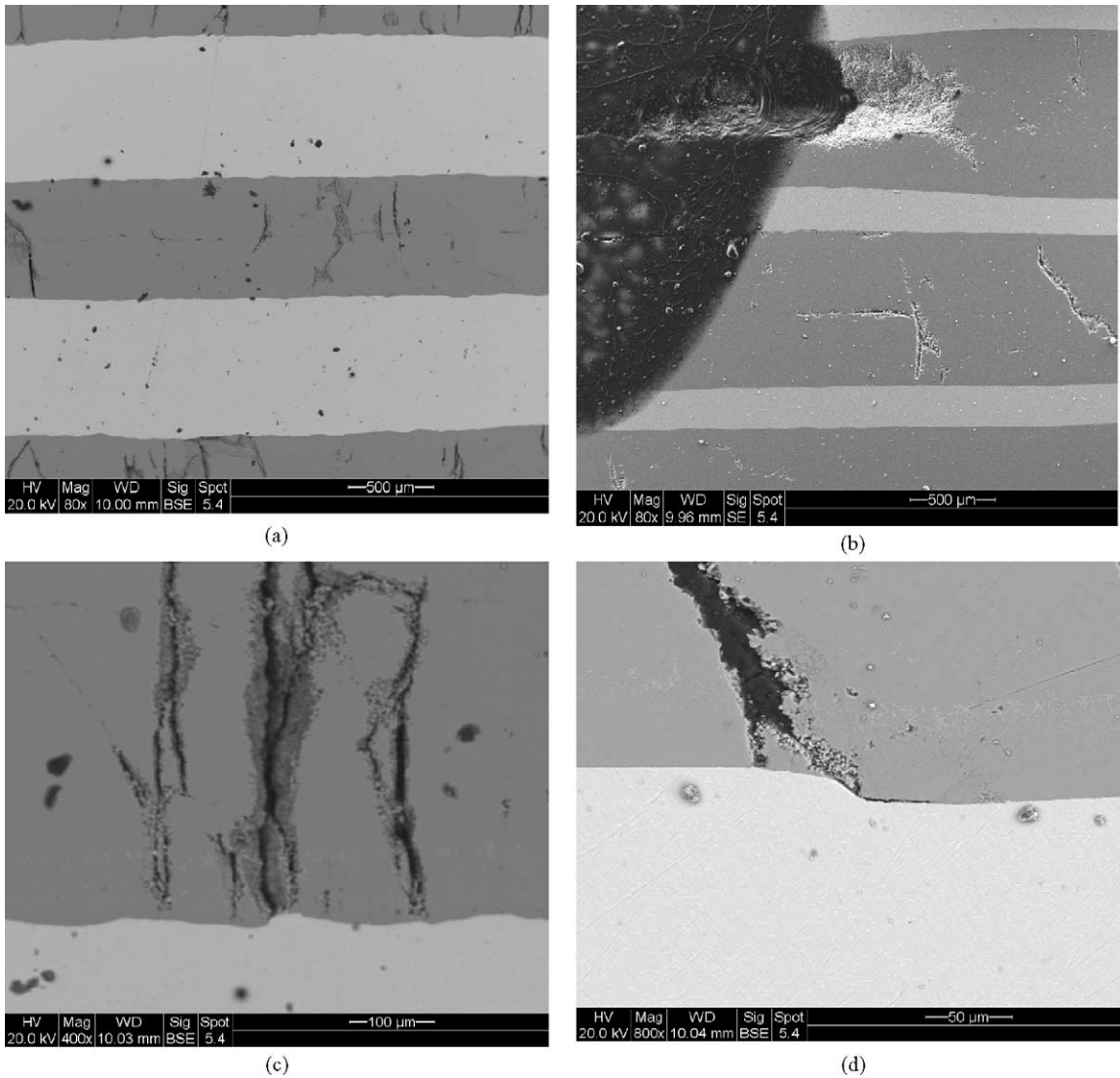


Fig. 8. SEM, perpendicular compression: (a) 50% Ti-6Al-4V,  $\dot{\epsilon} = 0.0001/s$ ; (b) 14% Ti-6Al-4V,  $\dot{\epsilon} = 0.0001/s$ ; (c) 50% Ti-6Al-4V,  $\dot{\epsilon} = 0.0001/s$ ; (d) 14% Ti-6Al-4V,  $\dot{\epsilon} = 0.0001/s$ .

Fig. 7a and b shows the perpendicular and parallel loading configurations. The designation refers to the orientation between loading direction and plane of laminates. All photomicrographs are oriented in the manner shown in Fig. 7a and b. For all the parallel configurations, confinement fixtures were used at the ends to minimize edge and end effects.

#### 4.1. Damage evolution as a function of the volume fraction of titanium

##### 4.1.1. Perpendicular loading for volume fractions of 14 and 50% Ti–6Al–4V

In the back scattered SEM micrographs, the light phase is the titanium alloy, whereas the darker phase is  $\text{Al}_3\text{Ti}$ . As shown in Fig. 8a and b, the 50% configuration does not fail by shear whereas the 14% configuration shows shear failure. Axial splitting of the  $\text{Al}_3\text{Ti}$  layer, with the formation of vertical cracks aligned with the loading direction, appears clearly in the first case whereas the main failure mode in the second one is shear. Since the specimens are tested under the same conditions, the volume fraction of titanium is thought to be a key factor in explaining the difference of failure mode. The thicker titanium layer has a greater resistance to shear localization. From Fig. 8c, it is clear that the cracks in  $\text{Al}_3\text{Ti}$  are arrested along the interfaces between  $\text{Al}_3\text{Ti}$  and Ti. One can see that the cracks in the 50% Ti case form along the loading axis and when reaching interfaces, stop, without propagating through the Ti layers or deflecting along the interfaces. On the other hand, when a crack reaches the interface in the 14% Ti specimen, it can initiate the formation of a shear band in the Ti layer, leading to shear failure (Fig. 8d).

##### 4.1.2. Parallel loading for volume fractions of 14% Ti–6Al–4V

The principal features are vertical cracks propagating along the  $\text{Al}_3\text{Ti}$  phase and buckling of the Ti–6Al–4V lay-

ers. These vertical cracks often run in the center of the intermetallic, along a plane with greater defects. This is a residue from the synthesis stage and impurities are segregated along the center plane. Fig. 9a shows a crack running along this plane and other side cracks parallel to it. Delaminations can also be seen along the interfaces. Fig. 9b shows a crack that initiated along the central plane in  $\text{Al}_3\text{Ti}$  and that is moving towards the Ti– $\text{Al}_3\text{Ti}$  interface. This process has been concluded in Fig. 10 and the clear propagation of the interfacial crack is shown.

The buckling of the Ti layers plays a pivotal role in this kind of fracture. Again, the thicker Ti layers are more resistant to buckling in accordance with the Euler equation:

$$P_{\text{cr}} = \frac{\pi^2 EI}{L^2} \quad (20)$$

where  $E$  is Young's modulus,  $I$  the moment of inertia, and  $L$  the length of the specimen. The moment of inertia increases with the cube of the thickness of the Ti lamella; the thicker the layers, the less tendency for buckling. Buckling of the Ti–6Al–4V layer is clearly seen in the left-hand side of Fig. 11a, which leads to the collapse of the  $\text{Al}_3\text{Ti}$  layer. The right-hand side shows a shear band in the metallic layer, and Fig. 11b shows a close-up of this feature.

#### 4.2. Damage evolution as a function of the strain rate

It is difficult to compare damaged specimens at different strain rates because the total strains are not controlled. For this reason, separate experiments at prescribed strains have to be performed. The perpendicular compression test was done under different strain rate, quasi-static ( $\dot{\epsilon} = 0.0001/\text{s}$ ) and dynamic ( $\dot{\epsilon} = 2800/\text{s}$ ), on 14% titanium and the results were observed using SEM. In Fig. 12a and b, axial cracks and shear cracks are observed, and the delamination is observed in both situations. However, as seen in Fig. 12b, the shear

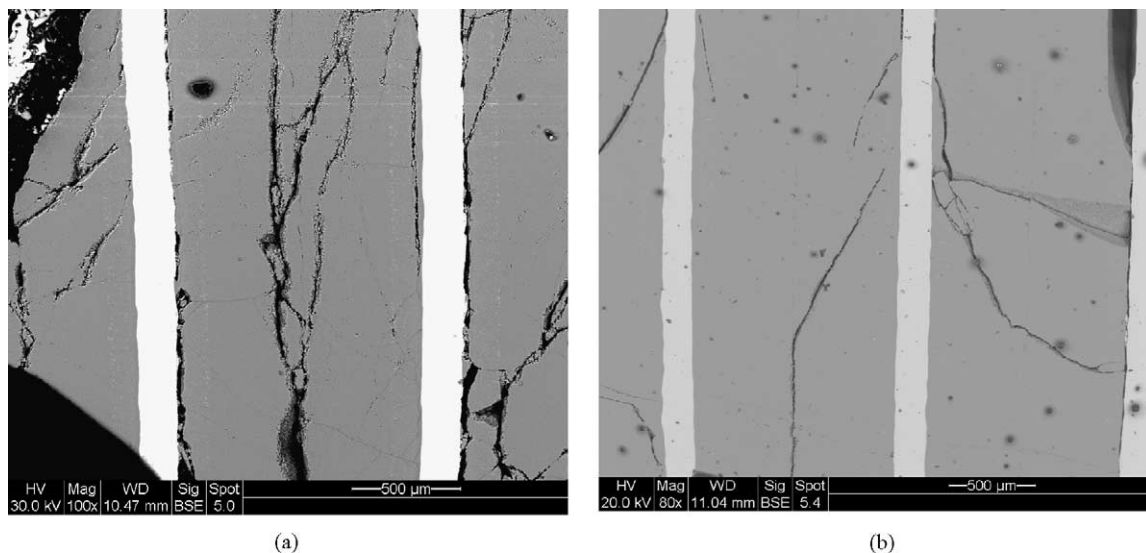


Fig. 9. SEM, parallel compression, 14% Ti–6Al–4V, with confinement: (a)  $\dot{\epsilon} = 2100/\text{s}$ ; (b)  $\dot{\epsilon} = 0.0001/\text{s}$ .

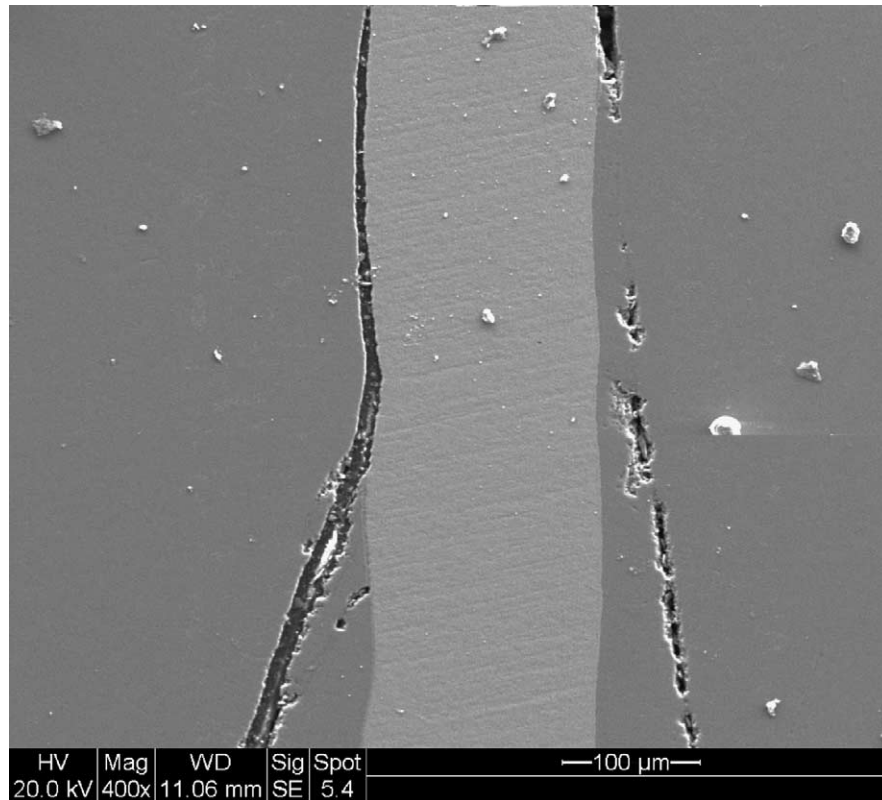


Fig. 10. SEM, parallel compression, 14% Ti-6Al-4V,  $\dot{\epsilon} = 2100/s$ , with confinement.

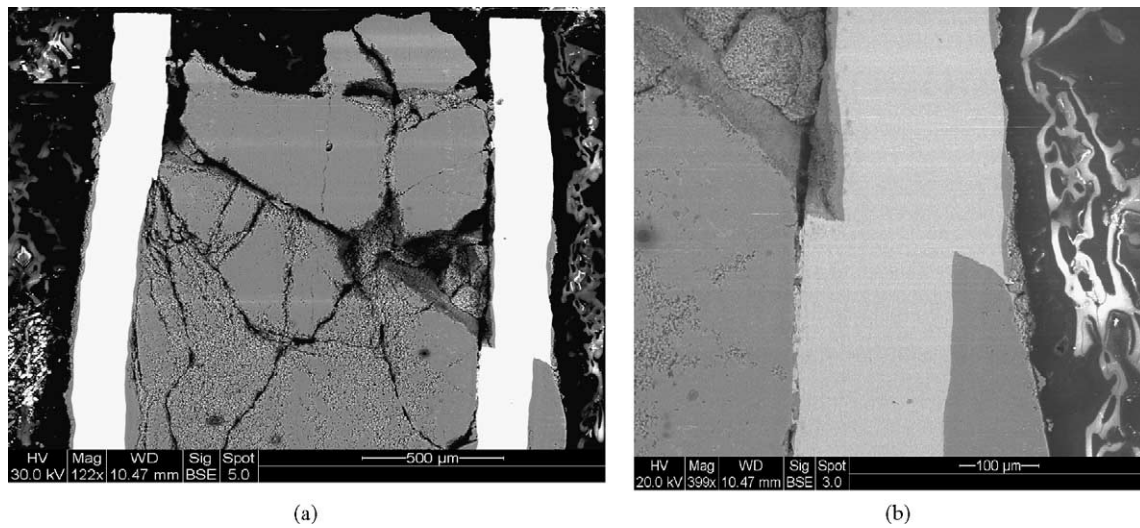


Fig. 11. SEM, parallel compression, 14% Ti-6Al-4V,  $\dot{\epsilon} = 0.0001/s$ , with confinement.

crack formed under quasi-static compression test in  $Al_3Ti$  layer continues till the Ti layer is also failed by shear, while in the dynamic test (Fig. 12a), the crack just deflects along the interface, leaving an intact Ti layer.

In conclusion, the MIL composite has higher strength in perpendicular compression than in parallel compression. MIL composite with 50% volume fraction of titanium is stiffer than the 14% one, and a higher strain rate seems to enhance the propensity to failure of MIL.

### 5. Damage evolution in Ti- $Al_3Ti$ metal–intermetallic laminate composites: physical modeling

The establishment of a failure criterion for the intermetallic layers in the MIL laminate requires a fundamental appraisal of the mechanisms of damage under the unique conditions experienced by  $Al_3Ti$ . The conventional failure mechanisms [27–29] are only strictly applicable to bulk materials, in which the three dimensions are of the same

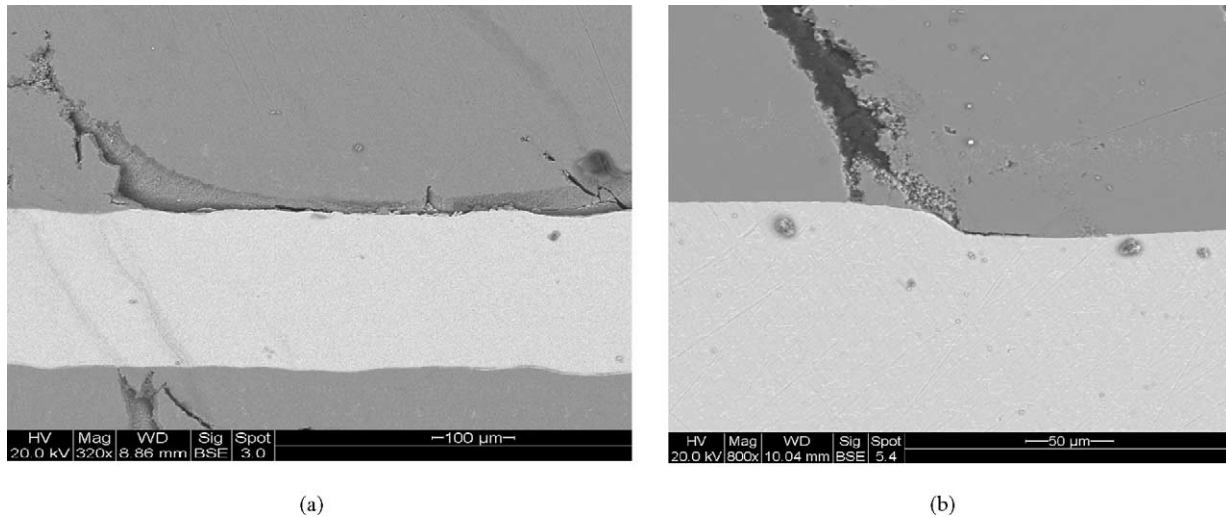


Fig. 12. SEM, perpendicular compression, 14% Ti-6Al-4V, with confinement: (a)  $\dot{\epsilon} = 2800/s$ ; (b)  $\dot{\epsilon} = 0.0001/s$ .

order. In the laminate, one of the dimensions is much smaller.

Hutchinson and Evans [30] and Evans et al. [31] have developed micromechanically-based damage mechanisms for multilayered materials. Some of these concepts are applicable to the MIL composites under study.

The interfacial strength is higher than the shear strengths of both metal and intermetallic, and therefore interfacial delamination is not a major failure mechanism [6]. The conclusions drawn from the observed results are given below.

### 5.1. Tension: parallel to laminate plane

Tensile cracks, perpendicular to the loading direction, and with a length equal to the thickness, appear with a decreasing spacing as the load is increased. This is shown schematically in the sequence shown in Fig. 13. The stresses are shown in the right-hand side. The external traction increases from (a) to (d). Each crack unloads the intermetallic, and this load transfer can be calculated [32]. As the spacing of cracks decreases, the load-transfer ability decreases and the metallic component carries a greater fraction of the load, leading to softening.

### 5.2. Compression: parallel to laminate plane

The intermetallic is confined between metallic layers, and therefore Poisson ratio effects can produce confinement stresses that affect the failure mechanism. Poisson's ratios for the intermetallic and metallic components are 0.17 and 0.32, respectively; if the metallic layer undergoes plastic deformation, its Poisson ratio is increased to 0.5. Thus, it is safe to assume that we have the scenario depicted in Fig. 14, i.e. the intermetallic will fail by shear. Fig. 14 shows three modes of damage accumulation: vertical cracks forming initially along the intermetallic central plane; buckling of the

metallic component (this initiates at the surfaces of specimen and propagates inwards); and shear band formation in Ti layer. From the SEM pictures (Fig. 11a and b), we can see clearly that under parallel compression loading, with the confinement, the Ti layer fails by buckling and shear localization. If the specimen is confined and axial splitting is inhibited, shear failure establishes itself as the dominant mode of failure. This is shown schematically in Fig. 15b.

### 5.3. Shear

This configuration was not tested in this program, but elements of shear failure are present in three point bending (or flexure) tests, that have been conducted [6]. For this external loading, tensile cracks at  $45^\circ$  to the interface should form. These cracks increase in density as the shear stress is increased, and they gradually unload the intermetallic layer. Fig. 16b shows this damage mechanism. Fig. 16c shows an alternative mechanism: a shear crack along central plane of  $Al_3Ti$ .

### 5.4. Compression: perpendicular to laminate plane

The sequence of damage accumulation that was observed in numerous experiments [6] is shown in Fig. 17. Damage initiates by the formation of axial splitting cracks in the intermetallic. These cracks are limited in size by the thickness of the intermetallic layer (Fig. 17b and c). Their spacing gradually decreases until they start connecting via shear failure in the Ti layer to the axial splitting cracks in adjacent layers. The damage thus evolves into shear failure because of the confinement provided by the Ti layers to the brittle intermetallic. This is confirmed by the SEM micrograph of Fig. 12b, where the cracks formed in  $Al_3Ti$  layer first develop a small "step" on the interface and then propagate through the titanium layer, which will ultimately form

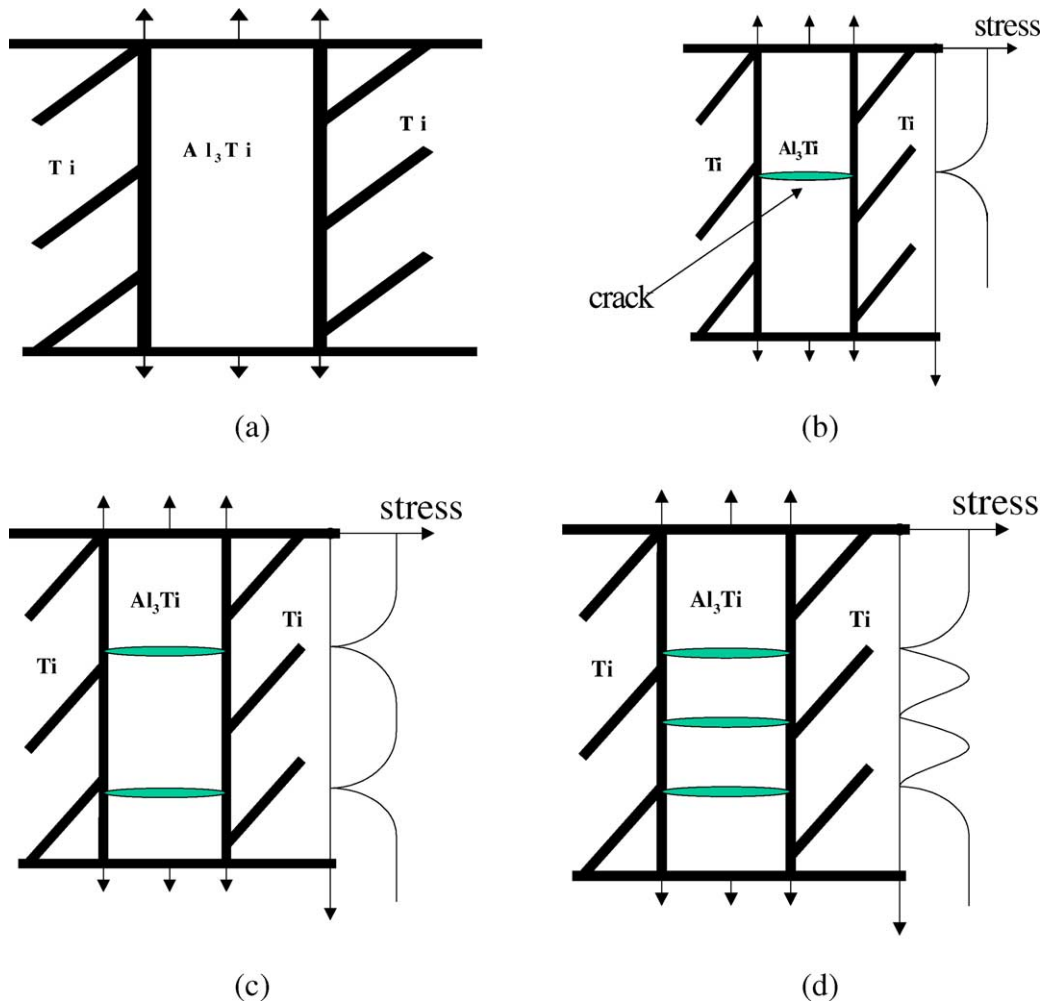


Fig. 13. Tensile loading parallel to laminate plane; increasing traction from (a) to (d).

the shear band Ti layer and lead to the final failure of the MIL.

## 6. Computational modeling

The intermetallic is modeled with the Johnson–Holmquist ceramic model [33] owing to the brittle nature of the Al<sub>3</sub>Ti, akin to ceramics and the Ti is modeled with the Johnson–Cook plasticity model [36]. While the Johnson–Holmquist model was originally developed for high strain rate ballistic applications, it works well across the full spectrum of strain rates used in the mechanical testing carried out in this project.

### 6.1. The Johnson–Holmquist ceramic model

Johnson and Holmquist [33,34] developed two ceramic models that are referred to in their subsequent work as JH-1 and JH-2. We are using the JH-2 version, which is summarized here. The stresses in the model are normalized by the

Hugoniot elastic limit (HEL) stress,  $\sigma_{\text{HEL}}$ , and the pressures are normalized by the pressure at the HEL,  $P_{\text{HEL}}$ . The normalized values have an asterisk as a superscript, i.e.  $\sigma^*$ .

The model describes the evolution of the damage in the material with a damage variable  $D$ , which ranges from 0.0 for the intact material to 1.0 for the fully fractured material. The normalized equivalent stress,  $\sigma^*$ , is linearly interpolated from the current values of the normalized intact and fractured strengths, which are subscripted with ‘in’ and ‘f’, respectively:

$$\sigma^* = \sigma_{\text{in}}^* + D(\sigma_{\text{f}}^* - \sigma_{\text{in}}^*) \quad (21)$$

The intact and fractured strengths are functions of the normalized pressure,  $P^*$ , and the normalized strain rate,  $\dot{\epsilon}^*$  (which is normalized by a reference strain rate).

$$\sigma_{\text{in}}^* = A(P^* + T^*)^N(1 + C\dot{\epsilon}^*) \quad (22)$$

$$\sigma_{\text{f}}^* = B(P^*)^M(1 + C\dot{\epsilon}^*) \quad (23)$$

$A$ ,  $B$ ,  $C$ ,  $M$ , and  $N$  are the material constants, which, for the purpose of initial computations, are taken as  $A = 0.85$ ,

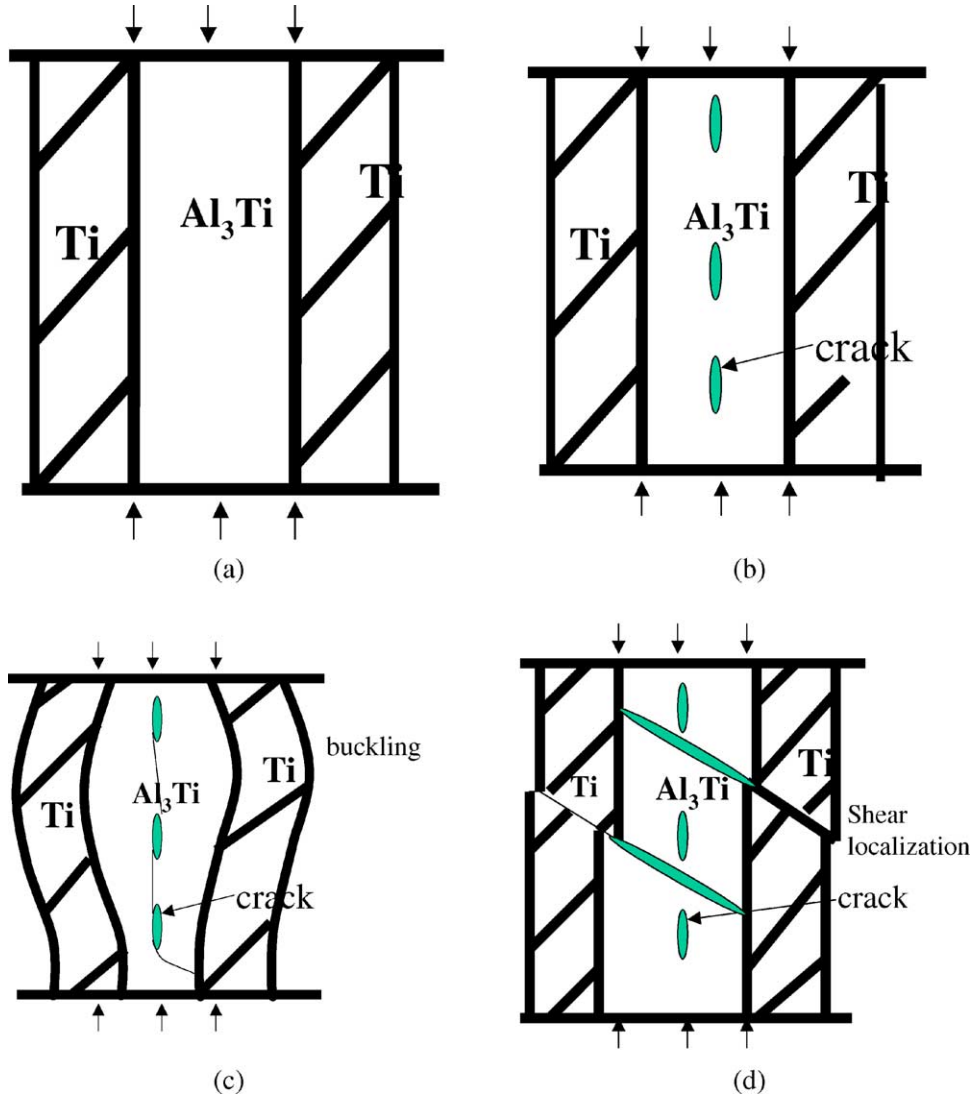


Fig. 14. Compression loading parallel to the laminate plane without confinement: (a) loading configuration; (b) axial splitting along central plane in  $\text{Al}_3\text{Ti}$ ; (c) plastic buckling of Ti; (d) shear localization of Ti.

$B = 0.31$ ,  $C = 0.013$ ,  $M = 0.21$  and  $N = 0.29$  from aluminum-nitride [35], due to the absence of these constants from Ti– $\text{Al}_3\text{Ti}$  MIL. As these constants are available later on, the computation will be refined accordingly. The maximum tensile hydrostatic pressure the material can withstand is  $T$ , and it appears in the intact strength as

$$T_{\text{HEL}}^* = T/P_{\text{HEL}}$$

The damage evolution is governed by an equation that is similar to the one used in the Johnson–Cook fracture model for metals [36], and it is expressed as

$$D = \sum \frac{\Delta \varepsilon_p}{\varepsilon_p^f} \quad (24)$$

where  $\varepsilon_p^f = D_1(P^* + T^*)^{D_2}$ .

The summation over the increments in the equivalent plastic strain,  $\Delta \varepsilon_p$ , is over the time steps, and  $D_1$  (0.02) and  $D_2$  (1.85) [35] are material constants.

In the range of pressures we are considering, the pressure is considered to be independent of the internal energy, or equivalently, the temperature. It is modeled simply as a polynomial in the compression,  $\mu = \rho/\rho_0 - 1$

$$P = K_1\mu + K_2\mu^2 + K_3\mu^3 \quad (25)$$

When damage accumulates in ceramics, bulking may occur, which is modeled in the Johnson–Holmquist model by adding an incremental pressure. Their bulking model is not used in the present calculations because we have found that it does not give us good results. A likely explanation is the presence of the titanium layers surrounding the intermetallic layers, which provides sufficient confinement to prevent the

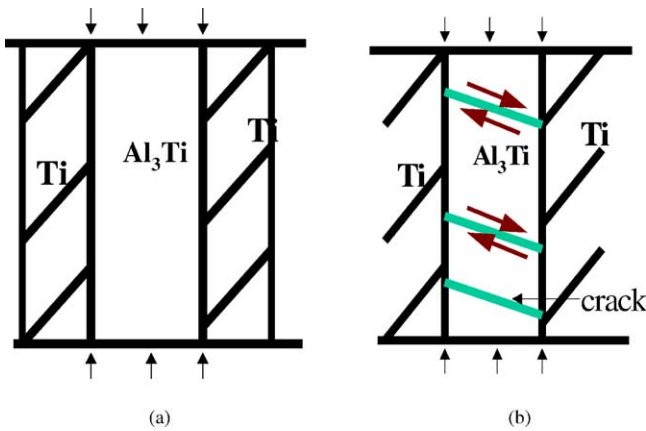


Fig. 15. Compression loading parallel to the laminate plane with confinement.

bulking behavior. This is highly desirable since researchers have long known that confinement improves the performance of ceramics.

Elements that have completely failed ( $D = 1$ ) are deleted from the calculation to model the cracking of the intermetallic. A special contact algorithm dynamically tracks the evolution of the new free surfaces created by the deletion of the elements and prevents the surfaces from penetrating through each other.

## 6.2. Finite element models

To validate the current material modeling effort by comparing the predicted results to the experiments, finite element calculations of the compression tests for strain rates of 1000 and 2000  $s^{-1}$ , and for quasi-static loading, were per-

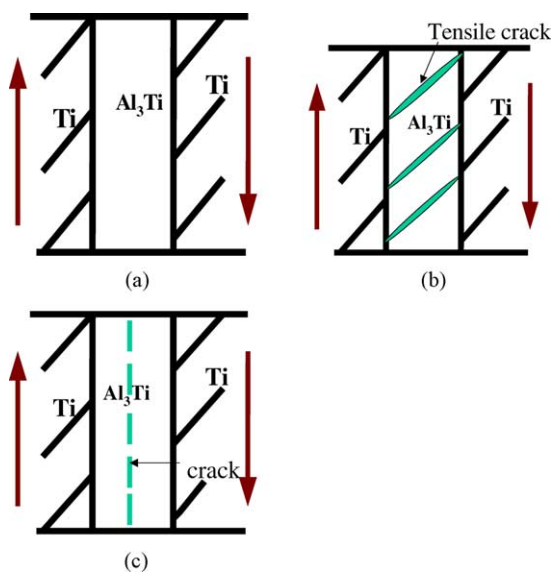


Fig. 16. (a) Shear loading parallel to laminate plane; loading configuration; (b) tensile cracks at 45° to interface; (c) shear crack along central plane of  $Al_3Ti$ .

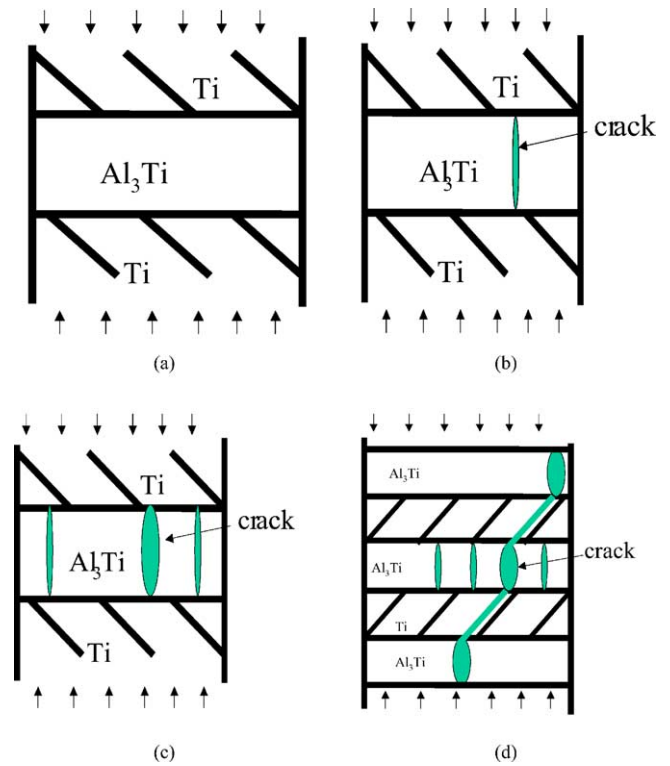


Fig. 17. Compression loading perpendicular to laminate plane; stress increases from (a) to (d).

formed. The calculations were performed in two dimensions because:

- previous calculations in three dimensions demonstrated that the third dimension was not important for the compression tests;
- two-dimensional calculations are easier for material designers to perform; and
- two-dimensional calculations require less time than three-dimensional ones, allowing broader parameter studies and faster design optimization.

Each layer of the MIL composite is modeled with several elements through its thickness for accuracy, with the precise number depending on the volume fraction of the titanium. The typical calculation has approximately 6000 elements. To maintain the same spatial resolution in three dimensions would increase the computational cost by a factor of 100. Corresponding to the experimental results, the Ti volume fractions in the calculations are 12, 20, and 50%. Quarter symmetry is used to reduce the model size, with the left and bottom boundaries having the symmetry conditions enforced. A rigid sample holder at the top boundary imposes the velocity boundary conditions that correspond to the specified strain rates. Compression tests in the directions perpendicular and parallel to the laminates were modeled, with the sample holder in the parallel case modified to impose a small amount of confinement at each end. This was done to

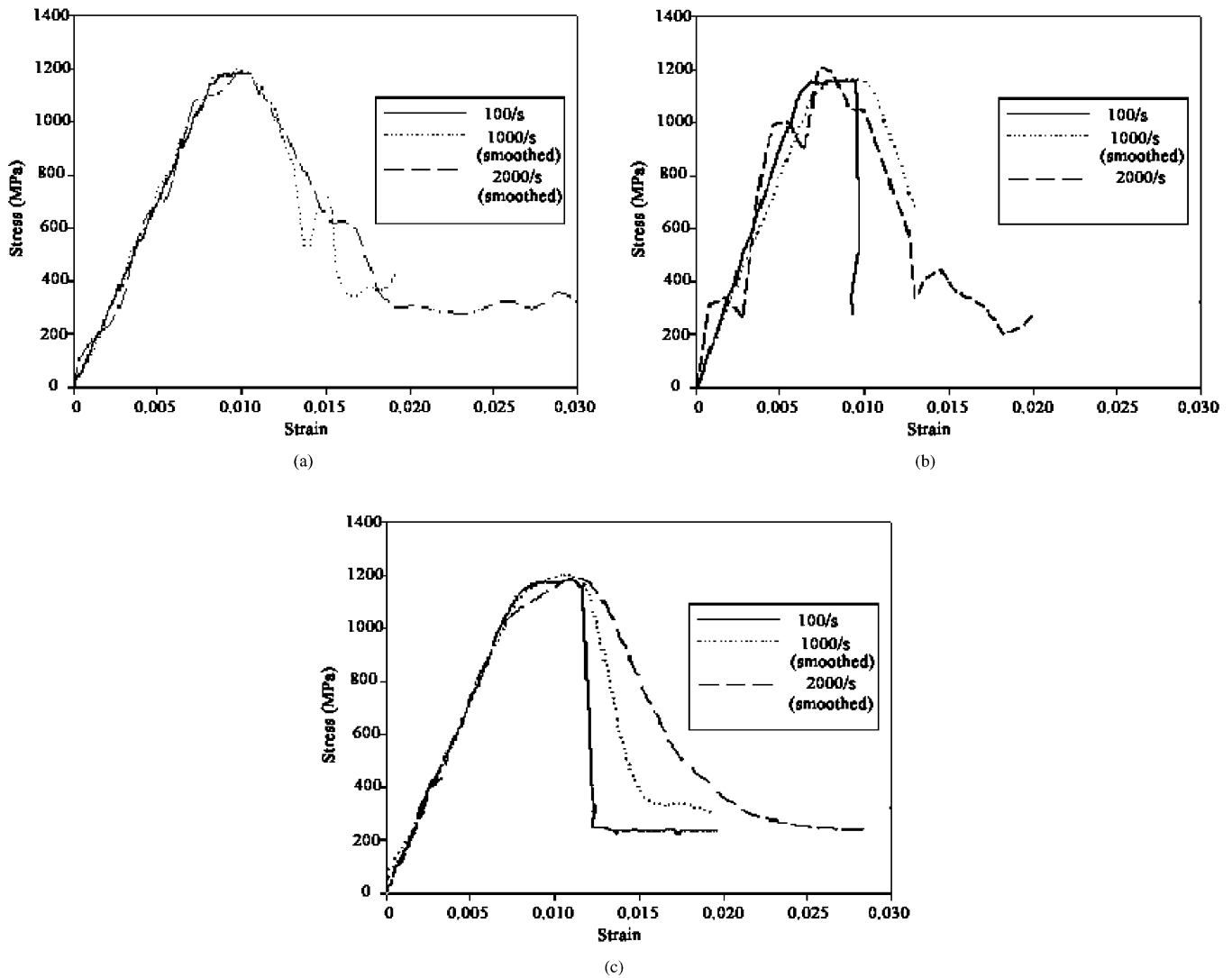


Fig. 18. Computational dynamic and quasi-static stress-strain curve, perpendicular loading: (a) 12% Ti-6-4 composite; (b) 20% Ti-6-4 composite; (c) 50% Ti-6-4 composite.

reflect the experimental procedure, where the confinement was found necessary.

### 6.3. Computational results

#### 6.3.1. The effect of titanium volume fraction on perpendicular compression tests

Nine calculations were performed for volume fractions of 12, 20, and 50% at strain rates of 100, 1000, and 2000. The strain rate at  $100\text{ s}^{-1}$  produces a response that is nearly quasi-static. The computation results are plotted in Fig. 18a–c, and the evolution of the internal fractures is shown in Fig. 19. In all cases we see that the peak stress is approximately 1200 MPa, which is the compressive strength of Ti-6-4 alloy. This indicates that the laminate material do not have strong rate sensitivity in the strain rate range tested here. The oscillations in the high strain

rate solutions are due to the stress waves splitting at the titanium–intermetallic interfaces. As the volume fraction of the titanium increases, the strain to failure increases from 0.01 to 0.013. The experiments have the same peak stress, but the strain to failure is almost a factor of 2 larger. There are two possible causes for this discrepancy.

- The values of damage evolution parameters  $D_1$  and  $D_2$  may need to be adjusted.
- The modeling of the cracks may artificially soften the material response. Elements that are deleted when they fail are no longer available to carry pressure loads in compression. This possibility will be investigated in the future.

We have concluded that the pronounced confinement effect of the titanium on the intermetallic is the underlying reason for the peak stress being independent of the titanium

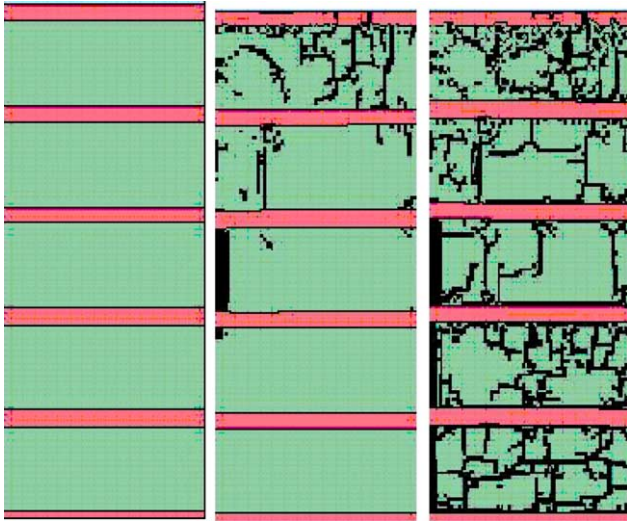


Fig. 19. Evolution of the internal fractures of 20% Ti-6-4 composite at  $\dot{\epsilon} = 1000/s$ .

volume fraction because the intermetallic, which has a compressive strength of 900 MPa and above, does not limit the compressive strength of the composite. This effect is evident in both the calculations and experiments. The material designer, therefore, is not constrained by the compressive strength in the perpendicular direction in determining the optimal volume fraction of titanium.

### 6.3.2. The effect of titanium volume fraction on parallel compression tests

The computations and experiments show that the failure mode in the parallel compression tests is the buckling of the titanium layers with the subsequent debonding and failure of the intermetallic layers. Euler beam buckling theory says that the buckling load increases with the thickness of the beam and decreases as the length of the beam increases. The results of the experiments are therefore highly sensitive to the specimen size (beam length) and the volume fraction of the titanium (beam thickness). While the results of experiments and calculations, discussed below, are interesting, they are not relevant to predicting the response of large plates of MIL composite.

The predicted strength of the composite is over twice the magnitude of the experimental value. We are confident that the reason for the discrepancy is the absence of imperfections (mainly in  $Al_3Ti$ ) in the computational model (see Fig. 20). A sequence of the evolution of the predicted failure mode is shown in Figs. 21 and 22. Note that the material fails near the holder, which is contrary to the experimental results. The buckling strength of a structure is extremely sensitive to seemingly small imperfections. The interface between the intermetallic and the titanium unquestionably has a small-scale waviness that substantially lowers the buckling load. This behavior has been seen before in other researchers' comparisons between predicted buckling

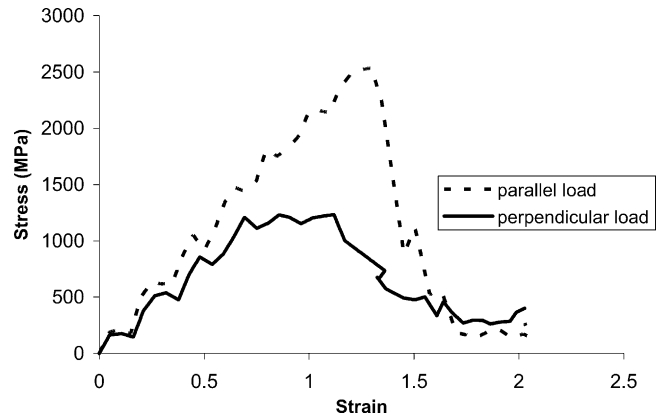


Fig. 20. Dynamic stress-strain curve of 20% Ti-6-4 composite at  $\dot{\epsilon} = 1000/s$ .

loads and the experimental results. In modeling the buckling due to blast loading, for example, SRI researchers found that they had to measure and model the imperfections in their test structure (an aluminum tube) otherwise the predicted deflections were only 30–50% of the measured values.

### 6.3.3. The effect of the titanium strength on the composite compressive strength

MIL composites can be manufactured using a variety of titanium alloys, and a parameter study was performed to determine whether or not using high performance alloys would benefit the overall performance of the composite. The study focused on a composite with a volume fraction of 20% titanium alloy, and subjected it to a compressive strain rate of  $1000 s^{-1}$ . We chose for baseline strength a value of 1092 MPa (150 ksi), which corresponds to Ti-6-4, and varied it in increments of 364 MPa (50 ksi) from 364

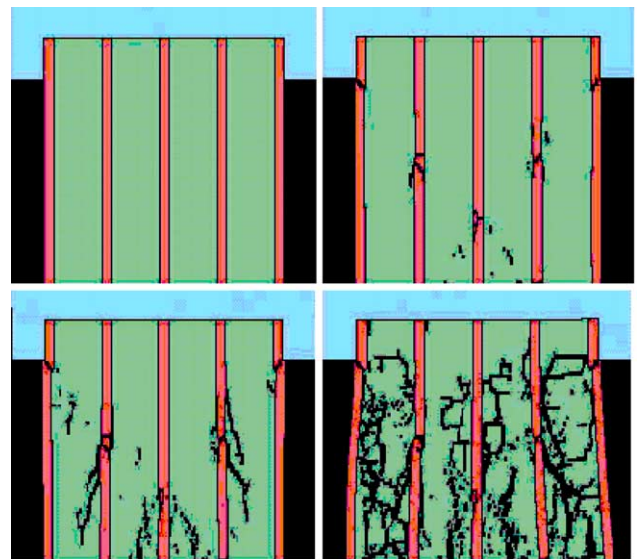


Fig. 21. Evolution of the internal fractures of 20% Ti-6-4 composite at  $\dot{\epsilon} = 1000/s$ ; parallel loading. The top and the bottom of the sample are confined.

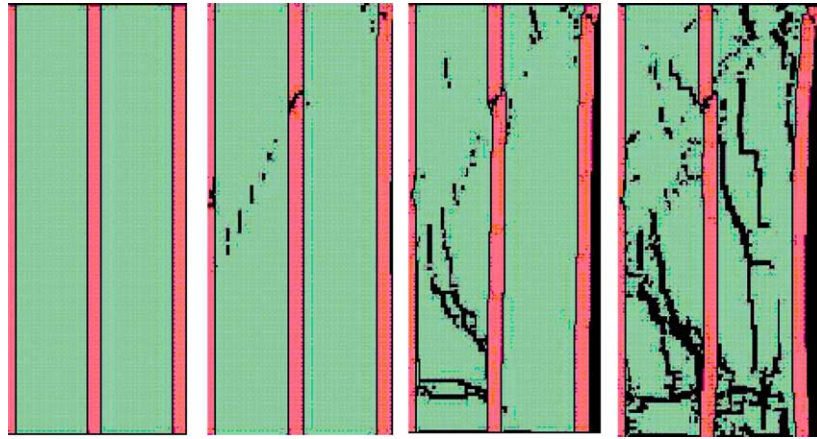


Fig. 22. Evolution of the internal fractures of 20% Ti–6Al–4V composite at  $\dot{\epsilon} = 1000/\text{s}$ ; parallel loading. The sample is not confined.

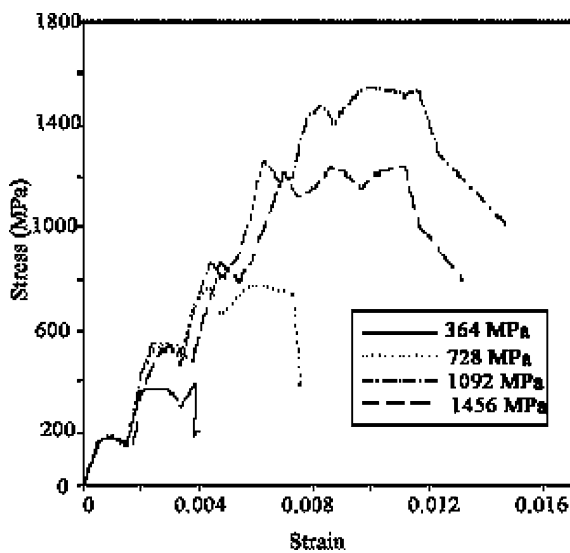


Fig. 23. Effect of the titanium strength on the compressive strength of 20% Ti composite at  $\dot{\epsilon} = 1000/\text{s}$ .

to 1456 MPa. Our results (Fig. 23) show that compressive strength of the composite is a nearly linear function of the strength of the titanium alloy, and is roughly equal to the titanium alloy as a design rule-of-thumb. This indicates that the cost of the MIL composite can be optimized by choosing an alloy appropriate to the structural loads, while retaining the ballistic performance enhancement associated with the intermetallic.

## 7. Conclusions

The goal of this investigation was to gain a greater insight into the mechanical strength of Ti–Al<sub>3</sub>Ti laminates synthesized through a novel process involving reaction between Ti and Al. Different tests, analysis and computations were performed which yield a predictive capacity of the lami-

nate performance as a function of fraction of the constituent Ti–6Al–4V and Al<sub>3</sub>Ti. The following principal conclusions can be drawn.

- The elastic anisotropy of this laminate is of the orthotropic kind, yielding Young's moduli ( $E_{11}$  and  $E_{22}$ ), Poisson's ratios ( $\nu_{12}$  and  $\nu_{23}$ ), and shear moduli ( $G_{12}$  and  $G_{23}$ ) are readily calculable as a function of Ti.
- The elastic properties were also calculated as a function of orientation. The calculated results are compared with the results of resonant ultrasound spectroscopy measurements for 20% Ti–80% Al<sub>3</sub>Ti, yielding good agreement.
- The stress intensity of the laminate was evaluated taking into account the residual stresses introduced by differences in thermal expansion coefficient between Ti and Al<sub>3</sub>Ti. A weight function method was used to compute the effect of the residual stresses on the fracture toughness.
- The damage in specimens compressed parallel and perpendicular to the layers was assessed and the following mechanisms were identified:
  - axial splitting;
  - shear localization in Ti layers;
  - crack propagation along the central plane of weakness in Al<sub>3</sub>Ti; and
  - delamination at Al<sub>3</sub>Ti–Ti interface.
- The damage evolution and strength were modeled using a 2D FEM code LS DYNA. The Johnson–Holmquist constitutive equation was used to model the brittle intermetallic and the Johnson–Cook equation for the Ti–6Al–4V. The compressive response when loaded perpendicular to the laminate planes match very well the compressive strength of the materials.
- The compressive strength of the composite is approximately equal to the strength of the titanium alloy over a broad range of alloy volume fractions. This indicates that the titanium alloy is very effective in confining the weaker intermetallic.

- (g) The ductility of the composite increases with the volume fraction of the titanium alloy. From the quasi-static to the dynamic regime (strain rate of  $2000 \text{ s}^{-1}$ ), the MIL composite exhibits very little strain rate sensitivity.

### Acknowledgements

Dr. L. Krueger provided valuable help in the early stages of this investigation. We also thank Dr. B. Ya, Dr. H.-H. Fu, Dr. Q. Xue, and Dr. B.K. Kad for specimen preparations and microscopy. Help from B. Cao, M.S. Schneider and J. Ma is highly appreciated. This research was supported by DARPA under Contract No. DAAD 19-00-1-0511 (Program Manager: Dr. L. Christodoulou) and Army Research Office under Contract No. DAAH04-96-1-0376.

### References

- [1] A.V. Virkar, J.L. Huang, R.A. Cutler, *J. Am. Ceram. Soc.* 70 (1987) 164–170.
- [2] K.L. Hwu, B. Derby, *Acta Metall.* 47 (1999) 529–543.
- [3] X.K. Peng, R. Wuhler, G. Heness, W.Y. Yeung, *J. Mater. Sci.* 34 (1999) 2029–2038.
- [4] M. Mitkov, D. Jankovic, D. Kicevic, *Materials Science Forum*, 1998, pp. 282–283.
- [5] J.C. Rawers, D.E. Alman, *Comp. Sci. Technol.* 54 (1995) 379–384.
- [6] A. Rohatgi, D.J. Harach, K.S. Vecchio, K.P. Harvey 51 (10) (2003) 2933–2957.
- [7] J.C. Rawers, H.E. Maupin, *J. Mater. Sci. Lett.* 12 (1993) 637–639.
- [8] J.C. Rawers, D.E. Alman, J.A. Hawk, *Int. J. Self-Prop. High Temp. Syn.* 2 (1) (1993) 12–24.
- [9] D.E. Alman, J.A. Hawk, A.V. Petty Jr., J.C. Rawers, *JOM* 46 (3) (1994) 31–35.
- [10] J.C. Rawers, J.S. Hansen, D.E. Alman, J.A. Hawk, *J. Mater. Sci. Lett.* 13 (1994) 1357–1360.
- [11] D.E. Alman, J.C. Rawers, J.A. Hawk, *Metall. Mater. Trans. A* 26A (1995) 589–699.
- [12] D.E. Alman, C.P. Dogan, J.A. Hawk, J.C. Rawers, *Mater. Sci. Eng.* A192–A193 (1995) 624–632.
- [13] D.J. Harach, K.S. Vecchio, *Metall. Mater. Trans. A* 32A (2001) 1493–1505.
- [14] R.M. Christensen, *Mechanics of Composite Materials*, Wiley, New York, 1990.
- [15] L.R. Calcote, *The Analysis of Laminated Composite Structures*, Van Nostrand Reinhold, New York, 1984.
- [16] C.L. Fu, *J. Mater. Res.* 5 (1990) 971–979.
- [17] J.E. Vuorinen, R.B. Schwarz, *J. Acoust. Soc. Am.* 108 (2) (2000) 574–579.
- [18] D.J. Green, *J. Am. Ceram. Soc.* 66 (11) (1982) 807–810.
- [19] V. Virkar, J.L. Huang, R.A. Cutler, *J. Am. Ceram. Soc.* 70 (3) (1987) 164–170.
- [20] D. Sherman, X. Gong, *J. Mater. Res.* 16 (3) (2001) 721–727.
- [21] D.J. Green, *J. Am. Ceram. Soc.* 66 (9) (1983) C178–C179.
- [22] R. Lakshminarayanan, D.K. Shetty, R.A. Cutler, *J. Am. Ceram. Soc.* 79 (1) (1996) 79–87.
- [23] J. Blattner, R. Lakshminarayanan, D.K. Shetty, *Eng. Fract. Mech.* 68 (1) (2001) 1–7.
- [24] T. Fett, D. Munz, *J. Mater. Sci. Lett.* 9 (1990) 1409–1416.
- [25] R.A. Cutler, A.V. Virkar, *J. Mater. Sci.* 20 (1985) 3557–3573.
- [26] T. Fett, D. Munz, *J. Am. Ceram. Soc.* 75 (11) (1992) 3133–3136.
- [27] M.A. Meyers, K.K. Chawla, *Mechanical Behavior of Materials*, Prentice-Hall, Englewood Cliffs, NJ, 1998, p. 154.
- [28] G.R. Johnson, T.J. Holmquist, *American Institute of Physics*, 1994, pp. 981–984.
- [29] S. Govindjee, G.J. Kay, J.C. Simo, *Int. J. Numerical Methods Eng.* 38 (21) (1995) 3611–3633.
- [30] J.W. Hutchinson, A.G. Evans, *Acta Mater.* 48 (1) (2000) 125–135.
- [31] A.G. Evans, J.W. Hutchinson, M.Y. He, *Acta Mater.* 47 (5) (1999) 1513–1522.
- [32] M.A. Meyers, K.K. Chawla, *Mechanical Behavior of Materials*, Prentice-Hall, Englewood Cliffs, NJ, 1998, pp. 656–663.
- [33] M.A. Meyers, L.E. Murr, K.P. Staudhammer, *Shock-Wave and High-Strain-Rate Phenomena in Materials*, Marcel Dekker, New York, 1992, pp. 1075–1081.
- [34] G.R. Johnson, T.J. Holmquist, in: S.C. Schmidt, et al. (Eds.), *High Pressure Science and Technology 1993*, AIP, New York, 1994.
- [35] T.J. Homquist, D.N. Templetm, K.D. Bishmoi, *Int. J. Impact Eng.* 25 (2001) 211–231.
- [36] G.R. Johnson, W.H. Cook, Presented at the Seventh International Symposium on Ballistics, The Hague, The Netherlands, 1983.